communications earth & environment

Article

A Nature Portfolio journal

https://doi.org/10.1038/s43247-025-03123-1

Substantial reduction of solar photovoltaic potential in China by an extreme dust event

Ke Yin[1,2,7], Fei Yao[3,4,7], Neng Luo[5], Meng Gao[6], Xiao Lu[1,2,8] ✉ & Bingqi Yi[1,2,8] ✉

Aerosols suspended in the atmosphere and deposited on solar panels reduce the solar power generation through dimming and soiling effects, respectively. Here we evaluate the impact of a six-day extreme dust event in March 2021 on the solar photovoltaic potential using an atmospheric chemical transport model integrated with a radiative transfer and a photovoltaic estimation module. The solar photovoltaic potential is found to be substantially reduced by up to 70% during this event, with the dimming effect accounting for 84-89% of the reduction and the soiling effect contributing about 16%. The estimated economic loss for the large-scale photovoltaic facilities in the affected regions is around 1.36 million American dollars, accounting for half of the installed capacity. Our results further reveal the intensified dust impact on photovoltaic potential under the control of anthropogenic emissions, which highlights the possibly stronger threat of future dust events on solar power generation under future cleaner atmosphere.

Renewable energy accounts for 30% of the world's primary energy (e.g., fossil fuels, wind power, and solar energy) supply in 2023[1]. Its share could rise to 30–40% by 2040[2], driven by the technical advances, cost cut, and encouraging policies aimed at accelerating the transition to cleaner energy sources[3]. Solar energy, as a widely applicable, abundant, and clean source of renewable power, is critically important in reducing the use of fossil fuel, curbing greenhouse gas emissions, and alleviating energy shortage[4,5]. Over the past decade, China has made remarkable progress in utilizing solar energy, reflected in the 130-fold growth of solar photovoltaic (PV) installations from 3 GW in 2011 to 393 GW in 2022, which accounts for 37.3% of the total PV installations over the globe in 2022[6]. As the carbon neutrality process advances, investigating the factors influencing solar power energy in China becomes increasingly important.

Using a solar PV panel is the predominant method for converting sunlight into usable electricity[7]. The diurnal solar cycle and cloud characteristics are the key factors affecting the solar radiation reaching the Earth's surface and the solar PV efficiency[8–11]. Besides, atmospheric aerosols also exert remarkable impacts[12]. On one hand, suspended aerosols in the atmosphere absorb and scatter sunlight, which attenuate the total radiation reaching the Earth's surface, thereby affecting the PV efficiency[13]. This effect is referred to as the dimming effect. On the other hand, aerosols deposit on the surface of solar PV panels and reduce the transmission of radiation to the panels, thereby reducing power generation efficiency. Such an effect is referred to as the soiling effect.

A number of studies have assessed the impacts of aerosols on the solar PV potential over different regions of the world[9,11,14–17]. The solar PV potential is commonly measured in terms of the plane-of-array irradiance (POAI) or the capacity factor (CF). For example, Bergin et al.[14] reported a reduction in CF by about 20% in arid and semi-arid regions such as the Arabian Peninsula due to dust emissions, and by 5–20% reductions in polluted areas of eastern China and northern India due to ions and organic/inorganic carbon. Using the surface solar irradiances from the Clouds and the Earth's Radiant Energy System (CERES) and the PVLIB-Python model, Li et al.[15] evaluated that the severe air pollution in East and North China led to a 25–35% reduction in the POAI from 2003 to 2014. Yang et al.[9] explored the differences in PV potential between southern China and northern India and found that cloud is the dominant factor in the former, while both aerosol and cloud are equally important to the POAI in the latter. Several studies further quantified the dimming and soiling effects of aerosols on solar PV potential separately. Li et al.[16] conducted a twelve-year (2003–2014)

[1]School of Atmospheric Sciences and Southern Marine Science and Engineering Guangdong Laboratory (Zhuhai), Sun Yat-sen University, Zhuhai, China. [2]Key Laboratory of Tropical Atmosphere-Ocean System, Ministry of Education, and Guangdong Provincial Observation and Research Station for Climate Environment and Air Quality Change in the Pearl River Estuary, Zhuhai, China. [3]National Centre for Earth Observation, University of Edinburgh, Edinburgh, UK. [4]School of Geosciences, University of Edinburgh, Edinburgh, UK. [5]Institute of Urban Meteorology (IUM), China Meteorological Administration, Beijing, China. [6]Department of Geography, Hong Kong Baptist University, Hong Kong, China. [7]These authors contributed equally: Ke Yin, Fei Yao. [8]These authors jointly supervised this work: Xiao Lu, Bingqi Yi. ✉e-mail: luxiao25@mail.sysu.edu.cn; yibq@mail.sysu.edu.cn

study using multi-source satellite data and MERRA-2 dataset and found that the aerosol soiling effect had a greater impact on PV potential than the dimming effect. Using a global chemical transport model coupled with a module for PV calculation, Yao et al.[17] also highlighted the relative impacts of dimming and soiling and further found that the global spatial variations in PV potential from 2008 to 2017 were mainly driven by precipitation and aerosol composition.

The abovementioned studies mainly focus on the impacts of aerosols on PV potential over multi-year to decadal timescales, while very few studies have elaborated on the effects of the short-term but potentially more intense aerosol pollution events. A key scenario that has been overlooked is the extreme dust event, particularly in Northern China, where one of the major dust sources on earth resides, and frequent dust storms occur[18,19]. Large-scale PV power plants are typically located in arid or desert regions, which effectively avoids the encroachment on cropland[20,21] and enables large potential for PV development[22], but are prone to be influenced by the dust events. Extremely high concentrations of dust aerosols (e.g., over 500 ug m^{-3}) in the atmosphere can greatly reduce the solar radiation reaching the Earth's surface through absorption and scattering[23]. Additionally, a large amount of dust quickly deposits on the PV panels in a short-time period[24], and severely affects the PV power generation.

The impacts of dust event on PV potential are expected to become increasingly prominent in China, with reduction in anthropogenic aerosols driven by emission control, and with global warming[25–27]. During dust event, the contribution of dust particles to the total atmospheric aerosols becomes increasingly large in China, as anthropogenic aerosol concentrations decline due to stringent emission-reduction policies targeting primary pollutants[28]. Meanwhile, global warming tends to intensify the convection over deserts and boost strong dust aerosol emissions[26], leading to more frequent and more intense dust events. However, the reduction of the output capacities of large-scale PV power plant infrastructure by dust events is not properly quantified. It also remains unclear about how the dust impact on PV system change in the context of reduced anthropogenic air pollutants and global warming.

Here, we explore the impact of the most severe dust storm in the decade of 2011–2021, which occurred on March 2021, on the PV potential in China. We integrate satellite measurements of aerosol optical depths and the GEOS-Chem chemical transport model at a regional high-resolution domain to constrain and reproduce this dust event. The GEOS-Chem model is then coupled with the rapid radiative transfer model (RRTMG) and the PVLIB-Python module to estimate the impact of this dust event on solar PV power generation in China (Supplementary Fig. 1). The variations of the dust impact on PV potential under various dust emission intensities and different anthropogenic emission scenarios are further explored. This allows us to provide new insights into the interaction between anthropogenic and natural aerosols on the radiation budget and PV potential.

Results

The extreme dust event in March 2021: Observations and simulations

Figure 1a shows a snapshot of the dust event captured by the Moderate Resolution Imaging Spectroradiometer (MODIS) onboard Aqua satellite on 15 March 2021. The extensive dust plumes cover a vast portion of northern China, spanning an area of 3.8 million square kilometers, which is equivalent to approximately 40% of the total land area of China. The dust plumes initiate from the Gobi Desert (GD) region on 15 March, and are transported downwind to North China Plain (NCP) and northeastern China under the influence of Mongolian cyclone circulation, and last until 20 March[29].

The dust aerosol optical depth (DOD) is derived based on the MODIS Collection 6.1 Deep Blue algorithm aerosol retrieval products in March from 2011 to 2021. Figure 1b–d show the spatial distribution of DOD in China for March 2021, the ten-year average (2011–2020), and the DOD anomaly in 2021, respectively. It is observed that the intensity of the 2021 dust event is unprecedentedly strong in the past decade. High DOD values (i.e., DOD > 0.5) are mostly limited over Northwestern China (NWC) in March on average (Fig. 1c), while particularly high DOD values which are approximately 2.5 to 5 times greater than average are found over the GD and NCP regions in March 2021 (Fig. 1b). The day-to-day variations of DOD for the individual years from 2011 to 2021 further illustrate that the March 2021 dust event exhibits record-breaking high DOD levels in the past decade over the GD and NCP regions (Fig. 1e–g). We thus focus on the impact of this extreme dust event on the solar PV in China.

The GEOS-Chem v12.9.3 chemical transport model coupled with the rapid radiative transfer module (GEOS-Chem-RRTMG) is used to reproduce the spatiotemporal distributions of dust concentrations, and to interpret the radiative impacts of the March 2021 dust event. The GEOS-Chem model simulates the emission, transport, chemistry, and deposition of dust aerosols at four separate size bins (at the radii of 0.1-1.0, 1.0-1.8, 1.8–3.0, and 3.0–6.0 μm) following Ginoux et al.[30] (2004). The smallest size bin is further divided equally into four submicron size bins (with effective radii centered at 0.15, 0.25, 0.4, and 0.8 μm) to improve the representation of optical properties and heterogeneous chemistry. In addition, the model accounts for the wet and dry deposition processes of aerosols depending on the size[31]. These processes are simulated on three-dimensional grids at the horizontal resolution of 0.5° × 0.625°, driven by MERRA-2 reanalysis meteorological data. Dust emissions are calculated using the Dust Entrainment and Deposition (DEAD) scheme, which depends on the surface wind speed, soil moisture, vegetation cover, and soil texture[32–35]. DOD is explicitly derived GEOS-Chem model based on the concentration, refractive indices, size distributions, and hygroscopic growth properties of dust particles. The simulation period ranges from 1 March to 21 March, 2021, with the first 14 days serving as the model spin-up period. More details on the model description and settings are provided in the *Methods* section.

The GEOS-Chem simulation using the standard code and default setting markedly underestimate the DOD in this dust event as compared with the MODIS-retrieved counterpart. As shown in Supplementary Fig. 2, the GEOS-Chem simulates a regional mean DOD of 0.18 over all three regions of interest (NWC, GD and NCP) during 15-20 March, which is 79% lower than that from Aqua MODIS retrieval. Such underestimation could result from the inaccuracies in the dust source used in the model[36,37]. Numerical models typically describe dust sources with static climatic distributions and ignore their dynamic evolution, while a dynamical adjustment approach to the dust source function is applied in this study (see the *Methods* section) to enhance the performance of model simulation before reliable quantification of dust impacts could be achieved (Supplementary Notes 1 and Supplementary Fig. 3).

Specifically, the DOD calculated on the basis of MODIS DB Collection 6.1 aerosol products are used to impose a top-down constraint on the dust concentrations simulated by the GEOS-Chem model. The overall strategy is to iteratively calculate the ratio of observed and simulated DOD for each model grid, and then apply this ratio to scale the dust source function at the corresponding grid in the GEOS-Chem simulation until the desired simulation accuracy is achieved (*Methods*). Over the entire dust event, we conducted a total of 83 iterative calculations to ensure the simulation error met the predefined accuracy threshold. The detailed description of the processes and results is summarized in the supplementary materials (Supplementary Fig. 3–5 and Supplementary Table 1). It is important to note that our method does not essentially improve the dust emission mechanisms in the GEOS-Chem model. Instead, it enforces the consistency between the model and observations by scaling the source function. Such an approach practically fulfills our aim to quantify the impacts of dust events on the solar PV potential, while further improvements to the dust emission process within the model are needed but outside the scope of this study.

Figure 2 shows the comparison of observed and simulated DOD in this extreme dust event after the top-down constraint. The optimized GEOS-Chem effectively captures the spatial distribution of observed DOD from the Aqua MODIS product during the dust event, with a modest regional averaged low bias of 13% (0.87 in observation vs 0.76 in GEOS-Chem) (Fig. 2a, b), as compared with the high bias of 85% before optimization

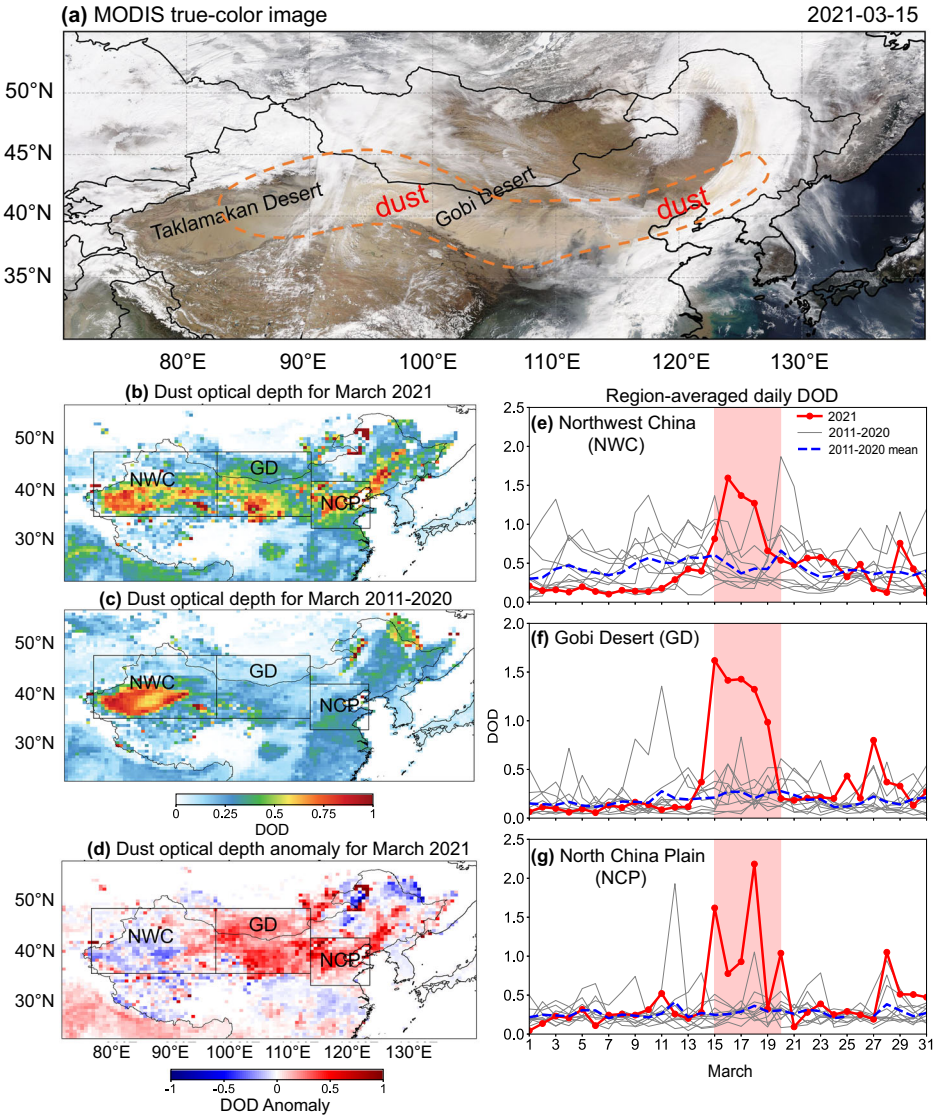

Fig. 1 | Observed extreme dust event on March 2021 in comparison with the climatology of 2011-2020. a shows the true-color image of the dust plumes captured by the MODIS Aqua on 15 March 2021. The orange dashed lines outline the area covered by the dust plume. **b**–**d** show the spatial distributions of DOD from MODIS Aqua (MYD08_D3) product for March 2021, March climatology (2011–2021), and their anomalies, respectively. The black boxes outline the three regions of interest, including the Northwest China (NWC, 36-47°N, 75-96°E), Gobi Desert (GD, 36-47°N, 96–112°E), and North China Plain (NCP, 34-42°N, 112-122°E). **e**–**g** show the time series of DOD averaged over the three regions. Daily regional mean DOD for March 2021 (red solid lines) is compared with the DOD for individual years in 2011–2020 (grey solid lines) and to the March climatology for 2011–2020 (blue dashed lines). The duration of the six-day extreme dust event is marked by the light red shading.

(Supplementary Fig. 2). The model also accurately reproduces the high DOD values (~3.0) observed in the NWC and GD regions, where dust particles accumulate due to air convergence induced by Mongolian cyclone[29]. Figure 2c–f further illustrate the daily variations in observed and simulated DOD during the dust event for the three individual regions and all regions. In addition to the Aqua MODIS data used for model optimization, we independently validate our results using Terra MODIS and VIIRS data obtained from the Suomi National Polar-orbiting Partnership (Suomi-NPP) satellite to address the potential limitations in temporal or spatial coverage from a single satellite product. The optimized GEOS-Chem model exhibited regional (NWC, GD, and NCP) averaged DOD biases of less than 16% (Fig. 2a and Supplementary Fig. 6) as compared with the satellite retrievals, with the temporal correlation coefficients (r) being 0.96, 0.84, and 0.86 for Aqua MODIS, Terra MODIS, and Suomi-NPP VIIRS, respectively (Fig. 2f). The model performs well in the NWC region, with the daily biases relative to Aqua MODIS being within ±20%. The simulated and observed DOD are 0.75 and 0.67, respectively, and are highly correlated with an r of 0.9 (Fig. 2c). In the GD region, GEOS-Chem also well captures the observed DOD daily variations with r ranging from 0.75 to 0.81, although the optimized simulation still shows a slight underestimation of approximately 10% as compared with that from Aqua MODIS (Fig. 2d). In contrast, the model exhibits a negative bias of 29% over the NCP, although it still captures the observed spatial distribution (Fig. 2e). The results suggest that the dust source function is not the sole factor influencing the simulated dust concentration in the model. Overall, the optimized GEOS-Chem model effectively reproduces the intensity and spatiotemporal evolution of this dust event, providing solid foundation for evaluating the dust influence on the solar PV potential.

Impacts of the extreme dust event on the solar PV potential and the associated economic loss in China

The GEOS-Chem coupled with RRTMG and the PVLIB-Python module is employed to calculate the solar PV potential over China and to quantify the impact of the March 2021 dust event (Supplementary Fig. 1). The PVLIB-Python with the *Erbs* module[38] (*Methods*) estimates the diffuse horizontal irradiance (DHI) and direct normal irradiance (DNI) from the global horizontal irradiance (GHI) simulated by GEOS-Chem-RRTMG, and calculates the irradiance components reaching the solar panels. The model also calculates the dust mass deposited on the surface of the solar panels and further estimated the irradiance reaching the cell module after being attenuated by deposited dust (Eqs. 5–8 in *Methods*), to derive the PV potential considering the environmental temperature and wind speed data. The simulated average surface downward direct shortwave irradiance under clear-sky conditions during the dust event are evaluated against the Clouds and the Earth's Radiant Energy System (CERES) Edition 4 A integrated irradiance (*Methods*). Results show that the model accurately reproduces

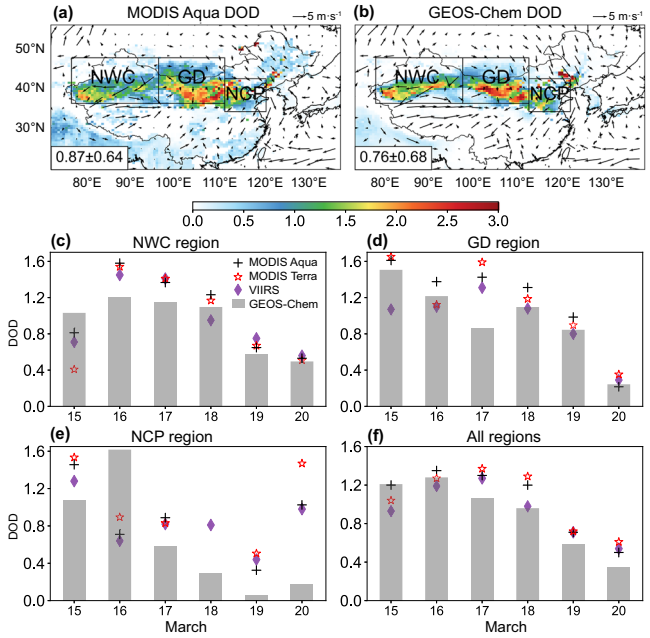

Fig. 2 | Evaluation of the spatiotemporal distributions of DOD simulated by GEOS-Chem model. Panels (**a**) and (**b**) show the spatial distribution averaged for 15–20 March, 2021 from the MODIS Aqua (MYD08_D3) product and GEOS-Chem simulation, respectively, overlaid with wind fields at 10 m (vectors; unit: m s^{-1}) obtained from fifth generation ECMWF reanalysis (ERA5) and the Modern-Era Retrospective Analysis for Research and Applications, Version 2 (MERRA-2) reanalysis dataset, respectively. **c**–**f** compare the daily variation of DOD from different satellite products (MODIS Aqua, MODIS Terra, and VIIRS) and GEOS-Chem simulations over three individual regions (NWC, GD, NCP) and the mean of the three regions.

the spatial distribution of surface downward direct shortwave irradiance during the dust event, where a high spatial correlation coefficient of 0.95 and a small normalized root mean squared error of 0.29 are found between the simulation and observation (Supplementary Notes 2 and Supplementary Fig. 7).

In this study, the capacity factor (CF) is calculated as the ratio of the actual PV electricity production during the dust event to the counterpart that could have been produced if the panels were not affected by the dust event and operated continuously at the design capacity (*Methods*). We consider three configurations of the PV panels, i.e., horizontal fixed (Flat), fixed with optimal tilt (Tilt), and one-axis tracking (OAT). The Flat panels are installed parallel to the ground, while the Tilt panels are installed at a fix angle, which depends on the latitude, to maximize the annual irradiance, and the OAT panels rotate around a single axis from east to west to track the sun, which results in the highest energy yield but comes with increased manufacture and maintenance costs. Figure 3a, c, and e show the spatial distributions of PV potential during the dust event which are derived from the GEOS-Chem-RRTMG-PVLIB modeling system under three configurations of PV panels, using the CF as a standard metric. In all configurations, the highest PV potential is found in the Tibetan Plateau, reflecting the impacts of the strong solar radiation (Supplementary Fig. 7), moderate cloud cover and low water vapor content, etc. Regions with relatively low PV potential include the Taklamakan Desert, Inner Mongolia, and the North China Plain, where dust emissions substantially reduce solar irradiance. Central China also exhibits low PV potential, primarily due to persistent cloud cover and high atmospheric water vapor content (Supplementary Fig. 8). Similar as previous studies[39,40], the spatial distribution of PV potential has been found to be primarily influenced by the incoming solar radiation at the top of the atmosphere, cloud cover, water vapor, and aerosols of natural and anthropogenic origins.

The CFs from the three configurations of PV panel show a similar spatial distribution, but their magnitudes differ considerably, due to the differences in the received GHI and the removal speed of the deposited dust from the surface of PV panels (Fig. 3a, c, e). We find that in low-latitude regions with high solar elevation angle, Flat and Tilt panels exhibit comparable CF values, peaking at 0.23 (Fig. 3a, c). In comparison, the OAT panel which dynamically aligns with the solar position could maximize the solar irradiance reception and elevate the maximal CF by 30% to 0.3 (Fig. 3c). By continuously adjusting the solar panel to face the sun, OAT configuration effectively reduces the solar radiation losses at low solar elevation angles, and shows greater advantages in mid- to high-latitude regions (e.g., the Tibetan Plateau and the GD and NCP areas), where the CF values range from 0.25 to 0.4 (Fig. 3e), exceeding those of Tilt (0.23-0.3) and Flat (0.18–0.23) configurations by up to 74%. These findings underscore the critical role of panel configuration in optimizing energy yield, particularly in regions with pronounced seasonal solar angle variations, which agree with the results from Li et al.[16] and Yao et al.[17].

Figure 3b, d, and f illustrate the quantified reduction in solar PV potential across China during the dust event, which is calculated as the difference in CFs between the model simulations with and without dust emissions. The mean CF reduction due to dust emissions (ΔCF_{dust}) and the attenuation ratio (ΔCF_{dust} divided by the regional averaged CF from the simulation without dust emissions) across the three sub-regions are presented in Supplementary Table 2. Under the three PV panel configurations, the spatial distributions of ΔCF_{dust} are similar but their magnitudes are different (Fig. 3b, d, f), with the OAT being the most affected one, followed by the Tilt and Flat cases. Notably, the Tilt panels show the greatest relative decrease (in percentage), whereas the OAT and Flat configurations exhibit nearly identical reductions. Although the magnitude of the ΔCF_{dust} differs among the three configurations of solar panels, the attenuation ratio remains similar, reaching up to 70% in the most affected regions in the NWC and the GD (Supplementary Fig. 9). We find that the magnitude of ΔCF_{dust} for different regions is generally proportional to the DOD levels, with the correlation coefficients between the two being 0.67-0.78 for different configurations of PV panels (Supplementary Fig. 10). Note March 15 and 16 exhibit the highest ΔCF_{dust}, which correspond to the days with the most intense dust storm influences (Fig. 2f and Supplementary Fig. 11).

Figure 4 further separates the total impact of the dust event on PV potential (Fig. 3b, d, and f) into the dimming and soiling effects. During the study period, the magnitude and spatial distributions of ΔCF_{dust} are predominantly determined by the dimming effect. The region-averaged dimming effects of the Flat, Tilt, and OAT cases account for 84%, 89%, and 88% of the ΔCF_{dust}, respectively, with the most affected regions being the NWC and GD regions, which is highly consistent with the spatial pattern of ΔCF_{dust}. In comparison, the region-averaged soiling effects account for 12-16% of the total ΔCF_{dust}. Dimming dominates along the dust plume pathway with substantial PV reductions, whereas soiling is weaker but more localized in downwind regions, highlighting the strong spatial variability in the relative contributions of the two processes. The strong dimming effects in the NWC and GD regions are primarily due to the high concentration of dust aerosols within the atmosphere. The pronounced soiling effect in the NWC region is primarily attributed to the absence of precipitation and elevated dust concentrations during this period (Supplementary Fig. 12), which facilitates the accumulation of deposited dust aerosols on PV panel surfaces, while the GD region records some precipitation that may mitigate the soiling effect when precipitation occurs[16].

Compared with the previous results, which suggest much larger soiling than dimming effects from the long-term perspective, our study reveals a contradictory result on the short-term scale. The discrepancy could be largely due to the different time frames of interest (i.e., days vs. years). Over the long timescales, aerosols in the atmosphere continuously deposit on PV panels and enlarge the soiling effect, especially in the absence of precipitation. Here, we analyze the relative importance of dimming and soiling effects during the dust event. The evolution of soiling effect indicates that its impact

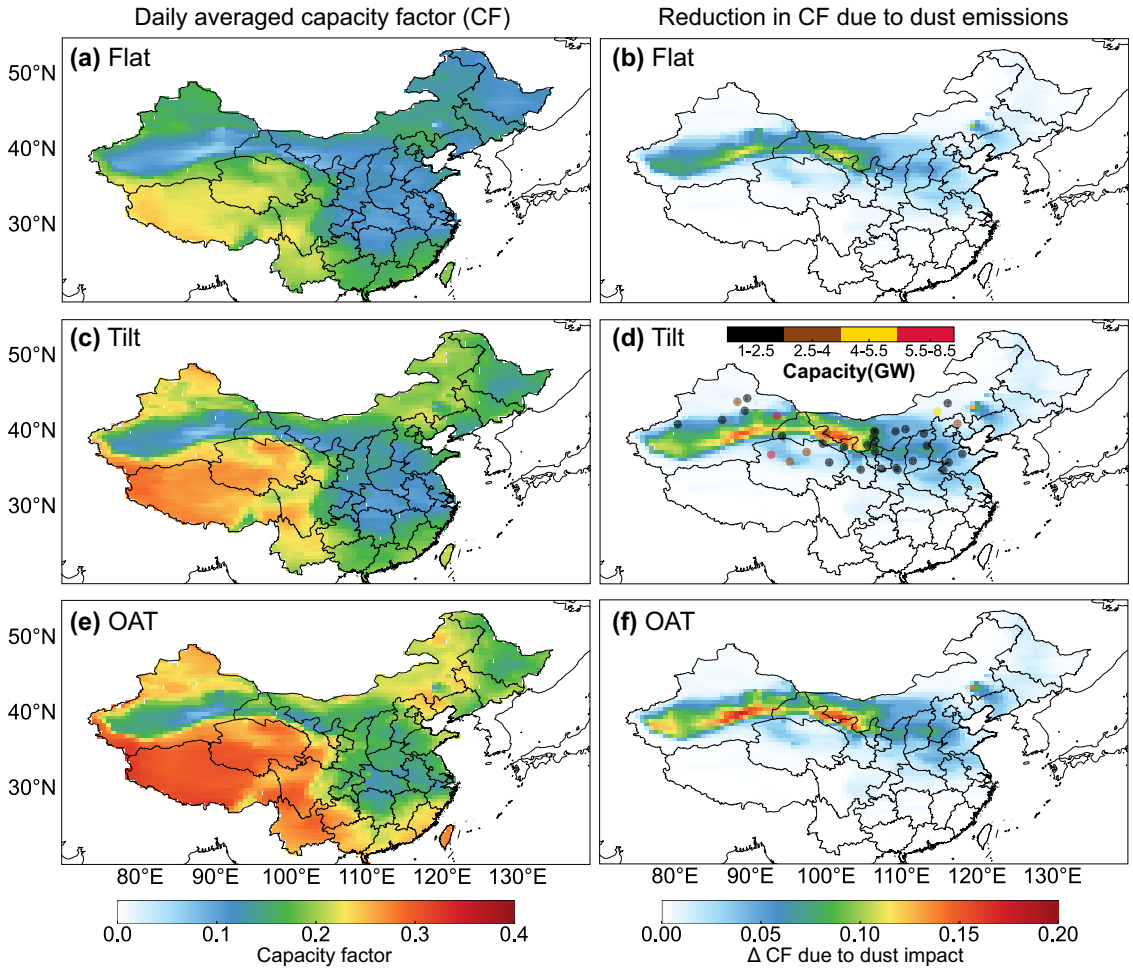

Fig. 3 | Capacity factor and its reduction induced by dust aerosols during the dust event (15-20 March). a shows the capacity factor derived by the GEOS-Chem-RRTMG-PVLIB model for the Flat panels. **b** shows the mean CF reduction due to dust emissions (ΔCF_{dust}). **c** and **d**, and **e** and **f**, are the same as **a** and **b**, but for the Tilt panel and OAT panel, respectively. Dots in **d** represent large PV plants (installed capacity over 1 GW) that are used to calculate the economic loss due the dust event.

could eventually surpass that of dimming (Supplementary Fig. 13). Our extended simulations, in which dust emissions were turned off after March 21, indicate that under the prevailing meteorological conditions, the effect of soiling becomes comparable to that of dimming around April 17 (about one month after the dust event) and surpass it onward (Supplementary Fig. 14). While the soiling effect tends to increase and become dominant in the long run, the dust event investigated here is both short in duration (~6 days) and unusually intense, with exceptionally high aerosol loading. Within such a short timescale, the total dust deposition remains limited[24]. Additionally, as PV technology continues to advance, various soiling mitigation approaches for solar PV power generation have been developed[41–44], making soiling a less prominent concern.

We now estimate the economic loss of this dust event due to its influence on the PV potential. The economic loss is defined as the financial loss caused by the reduction in power generation at the PV power plants due to the dust event. The dust event primarily affects the NWC, GD, and NCP regions, which collectively account for over 50% of the national PV capacity[6]. We analyzed 34 major centralized PV power plants in these regions (Supplementary Table 3) with an installed capacity exceeding 1 GW by the end of 2020[45] (Fig. 3d), which together account for 47% of the total PV installation in the three sub-regions. We first extract ΔCF_{dust} for each PV power plant, then calculate the lost energy by multiplying it by the duration of the dust event and the installed capacities, and finally determine the financial loss using the average electricity price for households in China in 2021[46]. We estimate that the dust event has caused a 21% reduction in CF averaged over the 34 major centralized PV power plants in these regions. This is equivalent to an economic loss of 1.36 million American dollars (≈16.5 GWh at electricity price of ~0.085 American dollar kWh^{-1}) during this event (Supplementary Notes 3). As the dimming effect dominates the overall ΔCF_{dust}, this loss is difficult to be prevented by cleaning the PV panels.

The nonlinear relationship between dust emission and photovoltaic potential attenuation

The above analyses demonstrate the large impacts of the extreme dust events on PV potential in China. Recent studies have shown that global warming has led to an increase in surface temperatures and a decrease in soil moisture, with drier soil contributing to an increasing trend in dust emissions[26,47,48]. Therefore, exploring the impact of stronger dust events on the PV potential becomes increasingly important for improving the power generation capacity of PV systems and mitigating potential economic losses caused by extreme weather events. In particular, the quantitative response of CF to dust concentrations has to be quantified for effectively projecting the dust impacts on the PV system.

Here we use the March 2021 event as the base scenario and assess the impacts of varying dust emissions on radiation and ΔCF_{dust} by scaling the dust emissions across all regions to 0%, 50%, 150%, and 200% of the original levels in each model grid. Although our simulations ignore the changes in dust distribution under various scenarios, quantified responses of the PV potential to the intensity of dust events could be derived. Only the results based on the OAT panel setting are presented since the responses of three configurations of PV panels are largely similar.

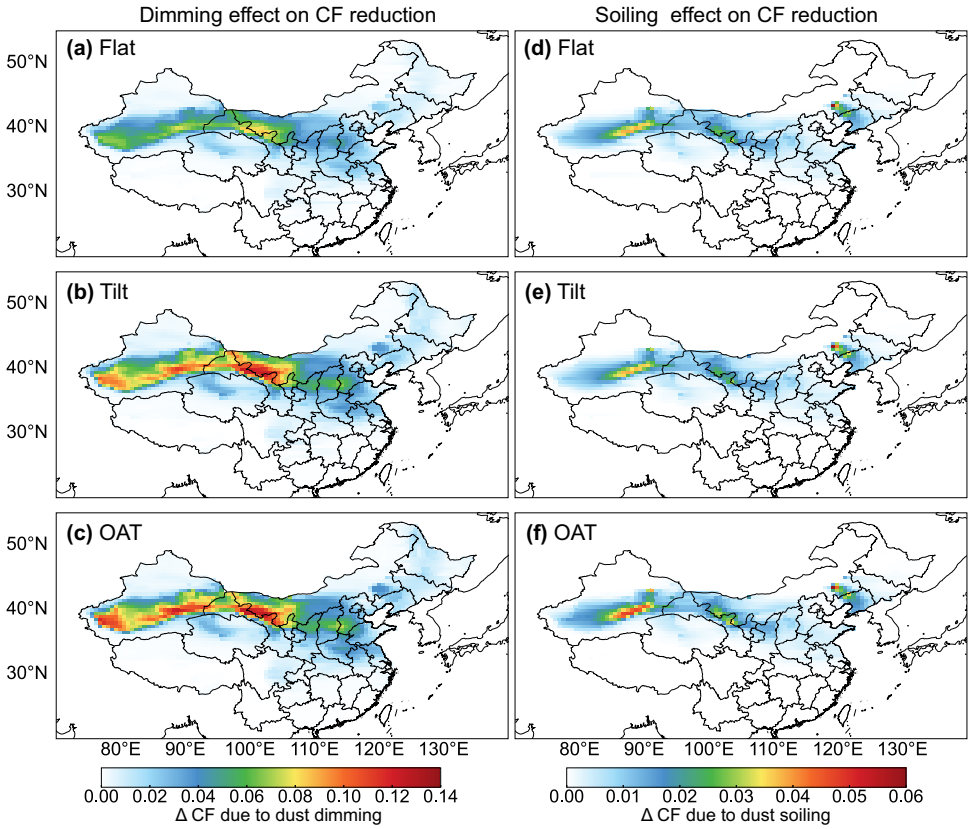

Fig. 4 | Contributions of dimming and soiling effect to the reduction of CF. a–c show the dimming effect and **d–f** show the soiling effect for the Flat, Tilt, and OAT panels, respectively.

Our results show that the simulated dust concentration first increases linearly as the dust emission increases, but is trending flat as the dust emission further grows (Fig. 5a). For example, when the dust emission rate increases to twice the level in the base scenario, the arithmetic mean dust concentrations averaged over the three regions rise by 89% from 1289 to 2446 μg m^{-3} with the combined influences of transport, chemistry, and deposition. Here, we additionally report the corresponding geometric mean and asymmetric confidence intervals as a robust measure for the data with a positive skew log-normal distribution containing heavy-tailed features and substantial spatial variability among the model grids. The geometric mean increases from 554 (95% confidence interval: 113 to 2705) μg m^{-3} in the base case to 972 (95% confidence interval: 177 to 5323) μg m^{-3} in the double emission case. In contrast, the radiation reduction caused by dust aerosols increases by only 35% from 38.8 to 52.5 W m^{-2} when the dust emissions double. It is found that although the dust concentration almost doubles in response to the double dust emission, the dust-induced radiation reduction first increases and then quickly converges and creases to further increase as the dust concentration increases, which is consistent with the Beer-Lambert law.

Figure 5b further illustrates the non-linear response of ΔCF_{dust} to dust emissions. It is observed that as dust emissions increase, the ΔCF_{dust} gradually increases as expected. However, the magnitude of the increase in ΔCF_{dust} gradually diminishes. When the dust emissions double the March 2021 level, the mean CF averaged over the NWC, GD, and NCP regions decreases by about 10% from 0.42 to 0.38 (an additional increase in ΔCF_{dust} by 0.04). The dimming and soiling effects have been found to account for 79% and 21% of the increase of 0.04 in ΔCF_{dust}, respectively. This indicates that the reduction in CF with increasing dust emissions is mainly driven by the dimming effect. As the dust emissions intensify, the dimming effect grows nearly linearly while the soiling effect experiences a slower but non-linear increase. The relative contribution of the dimming effect to the total CF reduction, however, slightly decreases at higher dust emission levels (Supplementary Fig. 15). In summary, the enhanced dust emission likely further reduces the PV potential in China, but the solar PV reduction does not monochromatically increase with the increase of dust concentration.

Enhanced impact of dust event on PV potential with lower anthropogenic emission

The aforementioned analyses have revealed the enhanced impact on PV potential with increasing intensity of dust event. However, even for the dust events of the same intensity, the concentrations and radiative effects of dust aerosol could be modulated through the heterogeneous chemical interactions between dust particles and ambient trace gases, such as NO_2 and SO_2. The ambient concentrations of NO_2, SO_2, and fine particulate matter ($PM_{2.5}$) have been substantially reduced with the implementation of air pollution control actions since 2013[49]. In this context, how the changes in anthropogenic air pollution level may influence the impact of dust event on PV potential remain unexplored. To address this question, we conduct four sensitivity simulations with the same dust emission of the March 2021 event, but under different scenarios of anthropogenic emission reductions over China (25%, 50%, 75% and 100% reduction).

Figure 6a displays the change in dust concentration when anthropogenic emissions of primary air pollutants (NO_x, SO_2, CO, VOCs, and primary particulate matters, etc.) are all removed under the same dust emission of the March 2021 dust event. Interestingly, higher dust concentrations are found in the absence of anthropogenic aerosols, with the national and regional (NWC, GD, and NCP) mean dust concentrations increasing by 3% and 13%, from 553 to 568 μg m^{-3} and from 1289 to 1452 μg m^{-3}, respectively. The corresponding geometric means increase from 72 (95% confidence interval: 7.5 to 705) to 74 (95% confidence interval: 7.47 to 730) and 554 (95% confidence interval: 113 to 2705) to 575 (95% confidence interval: 117 to 2808) μg m^{-3}, respectively. The regions with the largest increases in dust concentrations exist in the GD and NCP regions, and a few grids in the NWC region (Fig. 6a).

This can be explained by the fact that pollutants from various anthropogenic sources could increase the chemical removal of dust,

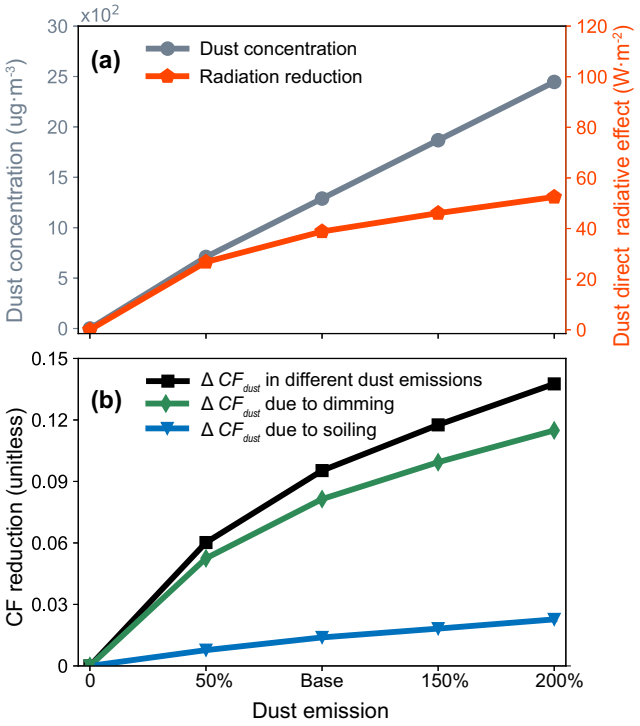

Fig. 5 | Response of dust concentrations and its impact on capacity factor to different intensity of dust emissions. a shows the response of the mean dust concentrations averaged over the three regions (grey solid lines) and surface shortwave radiation (red solid lines) to different dust emissions. **b** shows the response of total CF reduction due to dust emissions (ΔCF_{dust}) and the contribution from diming and soiling effect, respectively.

generating high-level soluble substances on the dust surface, which further lead to increased wet deposition of dust from the atmosphere[50]. In theory, dust particles absorb acidic gases such as HNO_3, SO_2, and H_2SO_4 through heterogeneous chemical reactions on their alkaline mineral surfaces, forming nitrate and sulfate coatings[31,51–55]. The GEOS-Chem simulations explicitly formula the formation of dust nitrate, dust sulfate, and dust alkalinity (the sum of calcium and magnesium carbonates) as separate size-segregated constituents in the model[31,55,56] (see Supplementary Notes 4 for key chemical reactions). Supplementary Fig. 16 clearly shows that dust sulfate and dust nitrate concentrations decrease by up to about 200 ppb and 6 ppb, respectively, when anthropogenic emissions of primary air pollutants are removed, compared to the base scenario. Our GEOS-Chem sensitivity simulation with doubled dust emissions also shows substantial decrease in NO_2 and SO_2 concentrations compared to the base scenario (Supplementary Fig. 17). These modeling results support that chemical interactions with dust and anthropogenic sources reduce the concentrations of both acidic gases and dust in the atmosphere. Previous study reported that the coatings not only consumed dust mass but also drove the dust aerosols more hydrophilic and effective cloud condensation nuclei (CCN), thereby enhancing wet deposition and reducing the amount of dust remaining suspended in the atmosphere[50,57–59]. As such, when anthropogenic emissions decline, this coating effect reduces, resulting in less dust being consumed through such chemical reactions and removal process. The GEOS-Chem model cannot account for these effects because it neither describes changes in hydrophilicity nor captures the role of dust as CCN. However, the model does simulate a decrease in total wet deposition of dust, dust sulfate, and dust nitrate by 5% and a dry deposition decrease of 12% when anthropogenic emissions are removed. This mainly reflects the changes in concentrations of dust sulfate and dust nitrate. Regionally, the larger increase in dust concentration with reduced anthropogenic emissions in the GD and the NCP than other regions reflect their higher emissions of acidic gases such as SO_2 and NO_2 (Supplementary Fig. 18), further supports the above mechanisms.

The increased dust concentrations with reduced anthropogenic emissions indicate that their impacts on the PV potential could enhance even at the same dust emission level. Figures 6b and 6c show the actual and relative changes of ΔCF_{dust} in response to the removal of all anthropogenic emissions in China. Regions with the largest change in the ΔCF_{dust} are in the GD and the NCP region, which is consistent with the changes in dust concentrations. In comparison, regions with the largest relative changes in CF ratio are not only in the GD region (up to 8%), but also in the north-eastern China (up to 9%) and in the central China (up to 14%). The ΔCF_{dust} Fig. 6d further summarizes the changes in dust concentrations and ΔCF_{dust} with reduction of anthropogenic emissions. With the reduction of anthropogenic emissions by 25%, 50%, 75%, and 100%, the ΔCF_{dust} over the GD and NCP regions increase by a maximum of 3%, 5%, 7%, and 8%, again reflecting the interactions between dust particulates and anthropogenic trace gases and aerosols. We note that the reduction of anthropogenic emission itself brings benefit for PV potential because the notable decrease in other aerosols leads to a much larger magnitude of CF increase than the ΔCF_{dust} (about five times larger than ΔCF_{dust} for the regional mean). Nevertheless, our results reveal that the impact of dust emissions on PV capacity could be amplified with the control of anthropogenic air pollutants, even if the intensity of dust emission remains the same, highlighting the need to consider the dust impact on the design and mitigation of PV power generation system in the future.

Discussion

By using the GEOS-Chem-RRTMG-PVLIB modeling framework constrained by DOD retrieved from MODIS satellite data, our analysis shows that the extreme dust event in March 2021—the most intense in China from 2011 to 2021—substantially reduces the PV potential by up to 70% across the NWC, GD, and NCP regions, which collectively account for over 50% of the national PV capacities. It results in an economic loss of approximately 1.36 million American dollars, highlighting the necessity to consider the impact of short-term extreme pollution events on the stability of solar photovoltaic energy generation. The reduction in dust-induced CF in this short-term event is dominated by the dimming effect (over 80%) rather than the soiling effect, which is apparently different from previous results that emphasized the soiling effect in long-term aerosol-induced PV potential degradation. We find that the impact of dust emission on PV potential could be enhanced with increasing dust emissions, but the curve flattens out at a certain dust emission. Furthermore, our findings demonstrate that the influence of dust on PV capacity intensifies alongside the reduction of anthropogenic air pollutants, even when dust emission levels remain constant. This amplification occurs because the reduction in anthropogenic emissions weakens the heterogeneous reactions between dust particles and anthropogenic acidic gases, thereby increasing dust concentrations and altering the dust radiative impacts.

Our results reveal the remarkable impacts of short-term extreme dust events on solar PV performance, which pose an immediate threat to the stable operation of existing solar PV power plants. Note the extreme dust events are defined as the dust events on the condition that (1) the regionally averaged DOD during the event exceeds the 90th percentile of daily DOD in the spring (March-May) season from 2000 to 2023; (2) the DOD in the duration of the dust event remains higher than the climatological mean DOD[60]. Such extreme dust events typically occur every few years although our results indicate that they can occur annually or at multi-year intervals. Between 2011 and 2021, extreme dust events in NWC occurred almost every 1–2 years with DOD values typically ranging from 1.0 to 1.7. In the GD, such events occurred about once every two years, with DOD mostly ranging between 0.5 and 1.0 and peaking at 1.37 in 2021. The NCP experienced the fewest events (only 4-5), but the 2021 event reached a peak DOD of 1.38, which is comparable to that in the GD (Supplementary Fig. 19). Our results also highlight the critical importance of incorporating dust-related considerations into the design and optimization of future PV

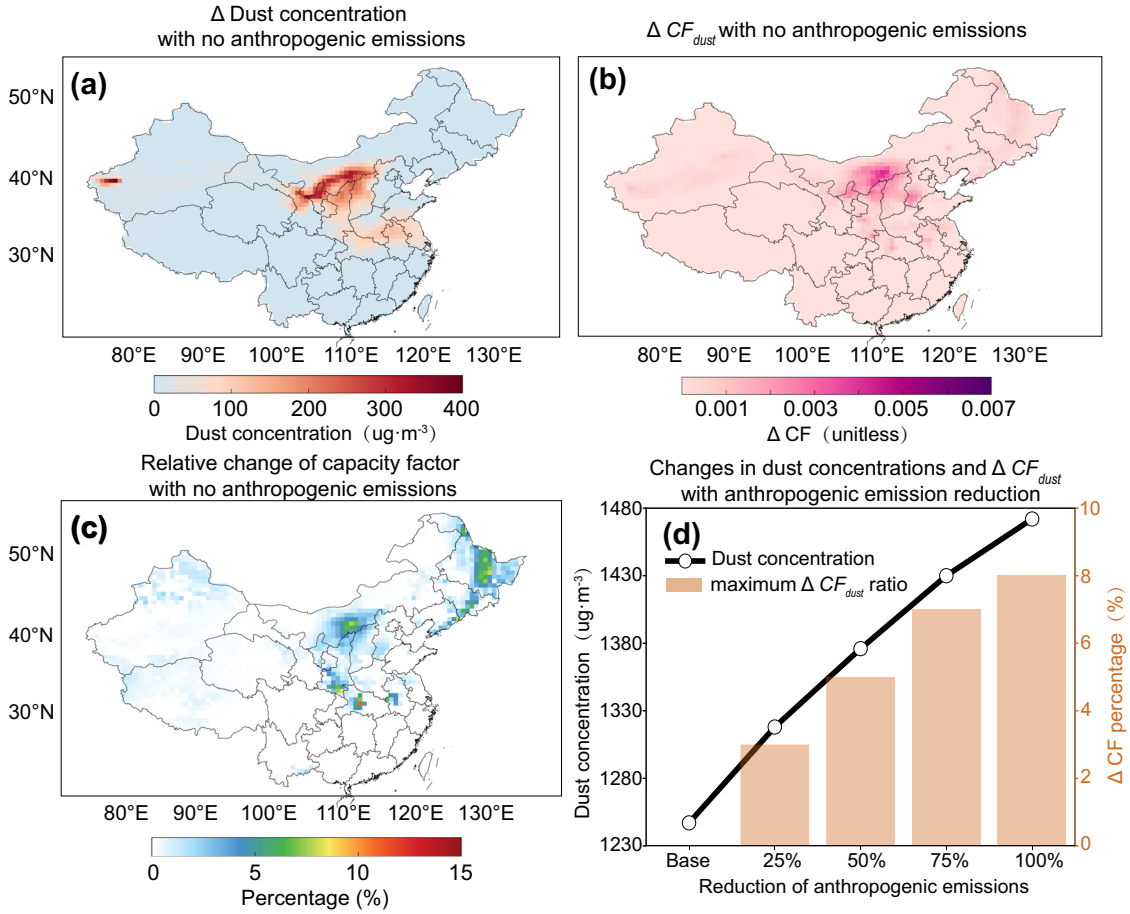

Fig. 6 | Response of dust concentration and its impact on capacity factor to different intensity of anthropogenic emissions. a shows the changes in dust concentrations for the 15-20 March 2021 case when all anthropogenic emissions are removed from the model. **b** and **c** show the corresponding changes in absolute magnitude and relative ratio of the dust-induced reduction in capacity factor (ΔCF_{dust}). **d** summarizes the changes in dust concentration (black lines, left y-axis) and increases in ΔCF_{dust} (orange bars, right y-axis) averaged over the three regions with reduction of anthropogenic emissions.

power systems, particularly in the context of continued control of anthropogenic emissions. Given that the impact of atmospheric dimming substantially exceeds that of soiling during the dust event, timely adjustments in power dispatch are recommended in response to dust storm forecasts. After the dust event ends, the gradual accumulation of soiling further underscores the need for prompt cleaning to restore PV performance to its rated capacity.

There are also some limitations in this study. For example, the changes in the environmental temperature with dust radiative forcing could further affect the power generation efficiency of PV panels, but such an effect is not considered in our calculation. Additionally, the offline GEOS-Chem-RRTMG simulation employed in this study could not account for the indirect radiative effect of dust on cloud formation[61,62]. The lack of real PV power plant data causes difficulties in the direct validation of the modeled energy losses. Inherently, our estimates are made based on radiative transfer calculations constrained by satellite retrievals, which inevitably induces uncertainties. Future work should integrate model simulations with on-site PV measurements to provide more robust assessments. More advanced weather–chemistry–energy coupled modeling systems could be used to improve the modeling performance. Moreover, it is worthwhile to investigate how the impacts of dust events could evolve in the context of global warming in the future world[26].

Methods

Satellite observations

We applied the dust aerosol optical depth (DOD) product, calculated from MODIS satellite data, to constrain and evaluate the GEOS-Chem simulation. The DOD data are obtained using the Deep Blue (DB) algorithm[63–65] from MODIS Level 2 aerosol data, which utilizes the radiance received by the blue channels to detect aerosol loadings over bright land surfaces (e.g., deserts). We use MODIS DB Collection 6.1 aerosol products from both the Terra (MOD04_L2) and Aqua (MYD04_L2) platforms and from Visible Infrared Imaging Radiometer Suite (VIIRS) on board the Suomi National Polar-Orbiting Partnership (SNPP) satellite. Before calculating DOD values, aerosol products including AOD at 550 nm (retrieved using the Deep Blue algorithm), single-scattering albedo (SSA), and the Ångström exponent were first interpolated onto a regular 0.5°×0.625° grid using the nearest-neighbor algorithm. Only AOD data flagged as good quality (quality flags: 2 and 3) were used. Following Pu and Ginoux[66], we separate the coarse-mode dust from the AOD:

$$\mathrm{DOD} = \mathrm{AOD} \times \left(0.98 - 0.5089\alpha + 0.0512\alpha^2\right) \qquad (\omega < 1, \alpha < 0.3) \quad (1)$$

where α is the Ångström exponent and ω is the SSA. The DOD is derived only when the ω is less than 1.0 and the α is below 0.3[29]. The setting of ω<1 mainly reflects the dust absorption of solar radiation, and effectively separates dust from other scattering aerosols such as sea salt aerosols[66]. The missing submicron dust aerosols have little impacts on the derived DOD as their fractions to total DOD are estimated to be small, typically on the order of ~1–5%[37].

We also applied the Clouds and the Earth's Radiant Energy System (CERES) (https://ceres.larc.nasa.gov/data/) integrated data product to evaluate the radiation output from GEOS-Chem-RRTMG. In this study, the CERES SYN1deg (Synoptic) Edition 4 A data provides all-sky and clear-sky

downward shortwave direct radiation data with a spatial resolution of 1° x 1° and a temporal resolution of 1 hour are used[67].

GEOS-Chem model coupled with the rapid radiative transfer model

We conducted a nested grid simulation using the GEOS-Chem v12.9.3 model coupled with the rapid radiative transfer model for general circulation models (GEOS-Chem-RRTMG), driven by Modern-Era Retrospective analysis for Research and Applications, Version 2 (MERRA-2) meteorological analysis. The model domain covers most regions of China (70°-140°E, 20°-55°N) at the resolution of 0.5° (latitude) × 0.625° (longitude). Boundary conditions are derived from global simulations at a resolution of 2° (latitude) × 2.5° (longitude) using the same setup of chemical and physical schemes. GEOS-Chem-RRTMG includes an advanced NOx-Ox-hydrocarbon-aerosol-bromine-chlorine-iodine mechanism for tropospheric chemistry, as well as dry and wet deposition mechanisms for aerosols and gases. The wet deposition mechanism includes convective updrafts, rainwater, and scavenging removal[68]. Dry deposition follows the on resistance scheme[69] and also considers the gravitational settling of aerosol particles[70]. The Community Emissions Data System inventory (CEDS v-2021-04-21) for the global anthropogenic emissions[71] and the Multi-resolution Emission Inventory for China (MEIC) for 2019 for China are used. The global domain simulations were conducted at 2° × 2.5° resolution from January 1 to March 21, 2021, with January and February serving as the spin-up period for the boundary conditions used to drive the nested model simulation. An additional 14-day spin-up (March 1–14) was applied for the nested domain simulations at the resolution of 0.5° × 0.625°. Such long spin-up time is sufficient given that the lifetime (relative to its transport and deposition) of dust in the nested model domain should be within 3–5 days. In addition, the use of assimilated MERRA-2 reanalysis meteorological fields as model input requires no spin-up time for climate conditions.

The model used the dust detrainment and deposition (DEAD) scheme[32] to simulate the dust event. The DEAD module in the GEOS-Chem uses the climatological land cover data from Advanced Very High Resolution Radiometer (AVHRR) to define the fraction of bare surface for the dust source function, which cannot reflect the dynamic changes in the dust source function caused by underlying surface variations[72] (e.g., bare or exposed soil can act as a source of dust, but not once it is covered by vegetation). The DEAD scheme[73,74] is based on the theory of wind-driven dust transport by White[75] to calculate horizontal dust saltation flux Q_S:

$$Q_S = C\frac{\rho}{g}U_*^3\left(1-\frac{U_{*t}}{U_*}\right)\left(1+\frac{U_{*t}}{U_*}\right)^2 \; if \; U_* > U_{*t} \tag{2}$$

where C is a global tuning factor determining the total dust strength, ρ is the air density, g is the acceleration of gravity, U_* is the friction velocity, and U_{*t} is the threshold friction velocity. The scheme calculates the vertical diffusion flux F as follows:

$$F = A_m S \alpha Q_S \tag{3}$$

where α is the sandblasting mass efficiency, which is a function of the clay fraction in the soil. Following Zender et al.[73], a fixed soil clay fraction of 0.2 is used in this study. S is the dust source function, which is the sand initiation probability function (also known as the wind erosion index) provided by the Georgia Tech/Goddard Global Ozone Chemistry Aerosol Radiation and Transport (GOCART) model which represents the distribution of potential dust source areas[37]. It is a quantitative factor derived by considering topographic variations, representing the distribution of potential dust source areas. A_m is a factor that suppresses dust emissions from snow covered land, wetlands and water bodies, and vegetated areas.

Based on the model-simulated atmospheric distributions and compositions of aerosols, the aerosol optical depth (τ) is calculated using their refractive indices, size distributions, and hygroscopic growth properties. The dust optical depth (DOD) is calculated using the following formula:

$$\tau = \frac{3QM}{4\rho r_e} \tag{4}$$

where ρ denotes the particle mass density, r_e is the effective radius and, Q is the extinction coefficient, derived from the single-scattering properties calculated using the refractive index and Lorenz-Mie code as well as the aerosol size distribution. Note both τ and Q are wavelength-dependent[76]. In this study, total AOD is calculated as the sum of the optical depths of sulfate, nitrate, ammonium, organic carbon, black carbon, dust, and sea salt, with the dust optical depth recorded separately to isolate the contribution of mineral dust.

To mitigate the underestimation of dust within the model simulation (Fig. S2), we utilized the calculated DOD from MODIS DB Collection 6.1 aerosol products to impose a top-down constraint on the dust concentrations simulated by the GEOS-Chem model. A dynamical adjustment to the dust source function was implemented to improve the model performance in this study, ensuring more reliable quantification of dust impacts. Our overall strategy is to calculate the ratio of DOD between satellite observations and model simulation for each model grid at the resolution of 0.5° × 0.625°, and then multiply this ratio to scale the dust source function (S) at the corresponding grid in GEOS-Chem simulation. The model is rerun iteratively until the simulated regional daily mean DOD falls within ±30% of the observed values, while ensuring accuracy and minimizing the number of iterative computations. We applied this method sequentially from west to east across the NWC, GD, and NCP regions, because this dust event originated in the NWC and GD regions, and the dust was transported eastward under the influence of a mid-latitude cyclone. As a result, modifications made to the simulations in the upstream regions could propagate to the downstream regions. We conducted the optimization for each day sequentially from 15 to 20 March. For instance, the restart file archived from the optimized simulation for 15 March is used to drive the simulation for 16 March, which was then further optimized based on observations on 16 March. More details are provided in the Supplementary Information.

The model uses the RRTMG scheme for radiation calculations. RRTMG is a fast radiative transfer model that uses the Correlated-K method[77] to handle atmospheric gas absorption and calculate atmospheric longwave and shortwave irradiances. The extinction sources considered in RRTMG include H_2O, O_3, long-lived greenhouse gases, aerosols, and others. For cloudy conditions, the Monte-Carlo Independent Column Approximation (McICA)[78] is used to handle the vertical overlap of cloud layers. RRTMG has been proven to have high accuracy in radiation transfer calculations, including extensive assessments of aerosol radiative effects[79,80].

PVLIB-Python Model

PVLIB-Python is an open-source Python library designed for PV system modeling and performance prediction. It offers a range of functions to analyze the performance of solar power generation systems, calculate irradiance, module temperature, power output, and more (https://pvlib-python.readthedocs.io/en/v0.10.3/index.html). The PVLIB-Python model applies different panel configurations to convert the solar radiation flux into the irradiance received by the solar panels, referred to as $POAI_{in}$. It then uses $POAI_{out}$ derived from $POAI_{in}$, along with the environmental temperature and wind speed from MERRA-2 meteorological analysis, to calculate the PV module temperature and effective irradiance. In this process, both the PV module efficiency (the efficiency of converting solar energy into direct current (DC)) and the inverter efficiency (the efficiency of converting DC into alternating current (AC)) are considered. We neglect the potential losses caused by factors such as module and inverter degradation. We use the capacity factor (CF) to describe the potential of photovoltaic power, defined as the ratio of the model simulated AC power to the AC power rating of the inverter (250 W) under standard conditions, following Yao et al.[17]:

$$\mathrm{CF} = \mathrm{AC}_{\mathrm{simulated}}/\mathrm{AC}_{\mathrm{designed}} \tag{5}$$

where $AC_{simulated}$ represents the simulated total power generation during the dust event and $AC_{designed}$ refers to the power generation under rating capacity.

We report results for three configurations of solar photovoltaic panels, i.e., horizontal fixed (Flat), fixed with optimal tilt (Tilt), and one-axis tracking (OAT).

Linking GEOS-Chem-RRTMG with the PVLIB-Python Model

The PVLIB-Python model is a community-supported tool that provides a wide range of functions and classes for simulating the performance of photovoltaic (PV) energy systems. Combined with the Erbs model[38], it can estimate Direct Normal Irradiance (DNI) and Diffuse Horizontal Irradiance (DHI) from Global Horizontal Irradiance (GHI) (Fig. S1). Using the calculated solar zenith and azimuthal angles, the model can further convert GHI, DNI, and DHI into the radiation available to the solar panel, including beam (E_b), ground-reflected (E_g), and sky-diffuse (E_d) components. Finally, the sum of these three types of radiation yields the irradiance received by the solar panel, referred to as the incident plane-of-array irradiance $POAI_{in}$.

Particulate matter (PM) deposited on solar panels further reduces the solar irradiance reaching the solar cells ($POAI_{in}$) where electricity conversion occurs. Following Bergin[14], we use broad-band-wise optical depth (τ) of deposited dust to calculate the solar irradiance used for PV conversion ($POAI_{out}$) as follows:

$$POAI_{out} = POAI_{in} \times e^{-\tau} \tag{6}$$

where τ is determined from the accumulated dry mass per unit area:

$$\tau = (E_{abs,d} + \beta_d E_{scat,d}) \times PM_d \tag{7}$$

where the subscript d denotes deposited dust. $E_{abs,d}$, $E_{scat,d}$, and β_d, and PM_d represent absorption and scattering mass extinction coefficients, the backscattering ratio, and the accumulated dry mass per unit area, respectively. The values of $E_{abs,d}$, $E_{scat,d}$, and β_d in the International System of Units are summarized in Table S4. We do not consider variations in extinction parameters for different PM species in this study due to the difficulty in implementing such a scheme to the model. PM_d refers to the net combination of dust accumulation and removal processes occurred on solar panels:

$$PM_d = PM_d^{Accum} - PM_d^{Removal} \tag{8}$$

PM_d^{Accum} comes from dust dry deposition processes:

$$PM_d^{Accum} = \int (V_d^{gra} \cos\theta_T + V_d^{tur}) C_d dt \tag{9}$$

where V_d^{gra} and V_d^{tur} are gravitational and turbulent dry deposition velocities for dust, respectively. C_d represents the surface dry mass concentration for dust. The value of C_d on Tilt solar panels is adjusted by applying a multiplication factor that depends on the tilt angle θ_T of the panels. Following Li[16], $PM_d^{Removal}$ shows a strong correlation with precipitation (p):

1) When $p < 1$ mm h^{-1}, no aerosol removal.
2) When $1 \le p < 3$ mm h^{-1}, organic carbon is removed by half, and sulfate is completely removed.
3) When $3 < p \le 5$ mm h^{-1}, dust is removed by half.
4) When $p > 5$ mm h^{-1}, dust is totally removed.

Model sensitivity simulations

Our Base simulation applies the aforementioned settings, including dust emissions and anthropogenic emissions, and with an optimized dust source (see text for details). Eight sets of sensitivity experiments were also conducted based on the Base simulation (Table S5). The Nodust simulation, with dust emissions turned off, is conducted to quantify the radiative effects of dust aerosols and explore their impact on PV potential by comparing the results with the Base simulation. To explore how the impact of dust on PV potential changes under different intensity of dust event scenarios in the future, we modified the dust emissions to 0.5, 1.5, and 2 times of that of the Base simulation, respectively. In addition, to investigate the impact of dust on photovoltaic potential under the same dust intensity scenario but with different anthropogenic emission levels, we reduce the anthropogenic emissions in China by 25%, 50%, 75%, and 100%, respectively.

Data availability

Aerosol Optical Depth (AOD) retrieved using the Deep Blue algorithm was obtained from the MODIS dataset and can be accessed at https://ladsweb.modaps.eosdis.nasa.gov/. MODIS true-color image is provided in https://worldview.earthdata.nasa.gov/. CERES SYN1deg (Synoptic) Edition 4 A datasets were obtained from https://ceres.larc.nasa.gov/data/. Our model output can be obtained upon reasonable request to the corresponding authors. The data results can be accessed from https://zenodo.org/records/17733351.

Code availability

GEOS-Chem codes can be accessed at https://github.com/geoschem/geos-chem. The PVLIB-Python codes can be accessed at https://pvlib-python.readthedocs.io/en/stable/. The other code is available from the corresponding author on reasonable request.

Received: 7 June 2025; Accepted: 9 December 2025;
Published online: 14 January 2026

References

1. IEA: World Energy Outlook (International Energy Agency, 2024). https://www.biee.org/meeting/iea-world-energy-outlook/ (accessed 30 January 2025).
2. Gernaat, D. et al. Climate change impacts on renewable energy supply. *Nat. Clim. Change* **11**, 119–125 (2021).
3. Bogdanov, D. et al. Radical transformation pathway towards sustainable electricity via evolutionary steps. *Nat. Commun.* **10**, 1077 (2019).
4. Li, T. et al. A radiative cooling structural material. *Science* **364**, 760 (2019).
5. Barthelmie, R. J. & Pryor, S. C. Potential contribution of wind energy to climate change mitigation. *Nat. Clim. Change* **4**, 684–688 (2014).
6. IRENA: International Renewable Energy Agency (IRENA), Renewable capacity statistics 2021. https://www.irena.org/publications/2021/March/Renewable-Capacity-Statistics-2021 (accessed 10 October 2024).
7. Crook, J. A., Jones, L. A., Forster, P. M. & Crook, R. Climate change impacts on future photovoltaic and concentrated solar power energy output. *Energy Environ. Sci.* **4**, 3101–3109 (2011).
8. Wild, M., Ohmura, A. & Makowski, K. Impact of global dimming and brightening on global warming. *Geophys. Res. Lett.* **34**, L04702 (2007).
9. Yang, J. Y. et al. Diverse cloud and aerosol impacts on solar photovoltaic potential in southern China and northern India. *Sci. Rep.* **12**, 19671 (2022).
10. Wang, L. C. et al. Hourly solar radiation estimation and uncertainty quantification using hybrid models. *Renew. Sustain.Energy Rev.* **202**, 114727 (2024).
11. Jiang, Y. H. & Yi, B. Q. An assessment of the influences of clouds on the solar photovoltaic potential over China. *Remote Sens*. **15**, 258 (2023).
12. Song, Z., Liu, J. & Yang, H. X. Air pollution and soiling implications for solar photovoltaic power generation: A comprehensive review. *Appl. Energy.* **298**, 117247 (2021).
13. Eltbaakh, Y. A. et al. Solar attenuation by aerosols: An overview. *Renew. Sustain. Energy Rev.* **16**, 4264–4276 (2012).
14. Bergin, M. H. et al. Large reductions in solar energy production due to dust and particulate air pollution. *Environ. Sci. Technol. Lett.* **4**, 339–344 (2017).

15. Li, X. Y. et al. Reduction of solar photovoltaic resources due to air pollution in China. *Proc. Natl. Acad. Sci. USA.* **114**, 11867–11872 (2017).
16. Li, X. Y., Mauzerall, D. L. & Bergin, M. H. Global reduction of solar power generation efficiency due to aerosols and panel soiling. *Nat. Sustain.* **3**, 720–727 (2020).
17. Yao, F. & Palmer, P. I. Source sector mitigation of solar energy generation losses attributable to particulate matter pollution. *Environ. Sci. Technol.* **56**, 8619–8628 (2022).
18. Kok, J. F. et al. Improved representation of the global dust cycle using observational constraints on dust properties and abundance. *Atmos. Chem. Phys.* **21**, 8127–8167 (2021).
19. Kok, J. F. et al. Contribution of the world's main dust source regions to the global cycle of desert dust. *Atmos. Chem. Phys.* **21**, 8169–8193 (2021).
20. Zhang, N. et al. Booming solar energy is encroaching on cropland. *Nat. Geosci.* **16**, 932–934 (2023).
21. Coimbra, C. F. M. Energy meteorology for the evaluation of solar farm thermal impacts on desert habitats. *Adv. Atmos. Sci.* **42**, 313–326 (2025).
22. Wang, Y. et al. Assessment of wind and photovoltaic power potential in China. *Carbon Neutral*. **1**, 15 (2022).
23. Kok, J. F. et al. Global and regional importance of the direct dust-climate feedback. *Nat. Commun.* **9**, 241 (2018).
24. Han, Z. W. et al. Model study on particle size segregation and deposition during Asian dust events in March 2002. *J. Geophys. Res.:Atmos.* **109**, D19205 (2004).
25. Xie, X. N. et al. Anthropogenic sulfate-climate interactions suppress dust activity over East Asia. *Commun. Earth Environ.* **6**, 159 (2025).
26. Zhou, Y. et al. Can global warming bring more dust? *Clim. Dynam.* **61**, 2693–2715 (2023).
27. Wang, F. et al. Arctic amplification-induced decline in West and South Asia dust warrants stronger anti-desertification toward carbon neutrality. *Proc. Natl. Acad. Sci. USA* **121**, e2317444121 (2024).
28. Sweerts, B. et al. Estimation of losses in solar energy production from air pollution in China since 1960 using surface radiation data. *Nat. Energy* **4**, 657–663 (2019).
29. Gui, K. et al. Record-breaking dust loading during two mega dust storm events over northern China in March 2021: aerosol optical and radiative properties and meteorological drivers. *Atmos. Chem. Phys.* **22**, 7905–7932 (2022).
30. Ginoux, P., Prospero, J. M., Torres, O. & Chin, M. Long-term simulation of global dust distribution with the GOCART model: correlation with North Atlantic Oscillation. *Environ. Modell. Softw.* **19**, 113–128 (2004).
31. Fairlie, T. D. et al. Impact of mineral dust on nitrate, sulfate, and ozone in transpacific Asian pollution plumes. *Atmos. Chem. Phys.* **10**, 3999–4012 (2010).
32. Meng, J. et al. Grid-independent high-resolution dust emissions (v1.0) for chemical transport models: application to GEOS-Chem (12.5.0). *Geosci. Model Dev.* **14**, 4249–4260 (2021).
33. Bruce, R. W. Soil transport by winds on Mars. *J. Geophys. Res.:Atmos.* **84**, 4643–4651 (1979).
34. Fairlie, T. D., Jacob, D. J. & Park, R. J. The impact of transpacific transport of mineral dust in the United States. *Atmos. Environ.* **41**, 1251–1266 (2007).
35. Bintanja, R., Severijns, C., Haarsma, R. & Hazeleger, W. The future of Antarctica's surface winds simulated by a high-resolution global climate model: 1. Model description and validation. *J. Geophys. Res.:Atmos.* **119**, 7136–7159 (2014).
36. Chen, Y. et al. A super dust storm enhanced by radiative feedback. *npj Clim. Atmos. Sci.* **6**, 90 (2023).
37. Ginoux, P. et al. Sources and distributions of dust aerosols simulated with theGOCARTmodel. *J. Geophys. Res.:Atmos.* **106**, 20255–20273 (2001).
38. Erbs, D. G. Estimation of the diffuse radiation fraction for hourly, daily and monthly-average global radiation. *Sol. Energy* **28**, 293–302 (1982).
39. Lu, Y. B. et al. Assessment of the high-resolution estimations of global and diffuse solar radiation using WRF-Solar. *Adv. Clim. Change Res.* **14**, 720–731 (2023).
40. Wang, Y. J. et al. Global spatiotemporal optimization of photovoltaic and wind power to achieve the Paris Agreement targets. *Nat. Commun.* **16**, 2127 (2025).
41. Khan, M. U. et al. Modeling and design of low-cost automatic self cleaning mechanism for standalone micro PV systems. *Sustain Energy Tech.* **43**, 100922 (2021).
42. Ilse, K. et al. Techno-economic assessment of soiling losses and mitigation strategies for solar power generation. *Joule* **3**, 2303–2321 (2019).
43. Guo, B. et al. Electrodynamic dust shield performance under simulated operating conditions for solar energy applications. *Sol. Energ. Mat. Sol. C.* **185**, 80–85 (2018).
44. Guo, B. & Javed, W. Efficiency of Electrodynamic Dust Shield at Dust Loading Levels Relevant to Solar Energy Applications. *IEEE J. Photovolt.* **8**, 196–202 (2018).
45. National Energy Administration, Statistics of photovoltaic power generation in 2020 (2020). http://www.nea.gov.cn/2020-07/31/c_139254346.htm (accessed 10 March 2025).
46. GlobalPetrolPrices.com. Electricity prices for households, September (2020). https://www.globalpetrolprices.com/electricity_prices/ (accessed 12 March 2025).
47. Wang, J. X. et al. Inherent spatiotemporal uncertainty of renewable power in China. *Nat. Commun.* **14**, 5379 (2023).
48. Cohen, J. et al. Linking Arctic variability and change with extreme winter weather in the United States. *Science* **373**, 1116–1121 (2021).
49. Geng, G. N. et al. Efficacy of China's clean air actions to tackle PM2.5 pollution between 2013 and 2020. *Nat. Geosci.* **17**, 987–994 (2024).
50. Fan, S. M. et al. Impact of air pollution on wet deposition of mineral dust aerosols. *Geophys. Res. Lett.* **31**, L02104 (2004).
51. Underwood, G. M. et al. Heterogeneous reactions of NO2 and HNO3 on oxides and mineral dust:: A combined laboratory and modeling study. *J. Geophys. Res.:Atmos* **106**, 18055–18066 (2001).
52. Tang, M. J., Thieser, J., Schuster, G. & Crowley, J. N. Uptake of NO3 and N2O5 to Saharan dust, ambient urban aerosol and soot: a relative rate study. *Atmos. Chem. Phys.* **10**, 2965–2974 (2010).
53. Li, L. et al. Kinetics and mechanism of heterogeneous oxidation of sulfur dioxide by ozone on surface of calcium carbonate. *Atmos. Chem. Phys.* **6**, 2453–2464 (2006).
54. Dong, X. Y. et al. Model development of dust emission and heterogeneous chemistry within theCommunity Multiscale Air Quality modeling system and its application over East Asia. *Atmos. Chem. Phys.* **16**, 8157–8180 (2016).
55. Zhang, L. et al. Improving simulations of fine dust surface concentrations over the western United States by optimizing the particle size distribution. *Geophys. Res. Lett.* **40**, 3270–3275 (2013).
56. Tian, R. et al. Exploring dust heterogeneous chemistry over China: Insights from field observation and GEOS-Chemsimulation. *Sci. Total Environ.* **798**, 149307 (2021).
57. Jha, V. et al. Sensitivity studies on the impact of dust and aerosol pollution acting as cloud nucleating aerosol on orographic precipitation in the Colorado River Basin. *Adv. Meteorol.* **2018**, 3041893 (2018).
58. Kumar, P., Sokolik, I. N. & Nenes, A. Measurements of cloud condensation nuclei activity and droplet activation kinetics of fresh unprocessed regional dust samples and minerals. *Atmos. Chem. Phys.* **11**, 3527–3541 (2011).
59. Krueger, B. J. et al. The transformation of solid atmospheric particles into liquid droplets through heterogeneous chemistry: Laboratory insights into the processing of calcium containing mineral dust aerosol in the troposphere. *Geophys. Res. Lett.* **30**, 1148 (2003).

60. Zhu, Q. Z. & Liu, Y. Z. The dominant factor in extreme dust events over the Gobi Desert is shifting from extreme winds to extreme droughts. *npj Clim. Atmos. Sci.* **7**, 141 (2024).
61. Zhou, M. et al. The impact of aerosol-radiation interactions on the effectiveness of emission control measures. *Environ. Res. Lett.* **14**, 2 (2019).
62. Zhao, B. et al. Enhanced $PM_{2.5}$ pollution in China due to aerosol-cloud interactions. *Sci. Rep.* **7**, 4453 (2017).
63. Sayer, A. M. et al. Validation, stability, and consistency of MODIS Collection 6.1 and VIIRS Version 1 Deep Blue Aerosol Data Over Land. *J. Geophys. Res.:Atmos.* **124**, 4658–4688 (2019).
64. Pu, B. & Ginoux, P. The impact of the Pacific Decadal Oscillation on springtime dust activity in Syria. *Atmos. Chem. Phys.* **16**, 13431–13448 (2016).
65. Gkikas, A. et al. ModIs Dust AeroSol (MIDAS): a global fine-resolution dust optical depth data set. *Atmos. Meas. Tech.* **14**, 309–334 (2021).
66. Pu, B. & Ginoux, P. How reliable are CMIP5 models in simulating dust optical depth? *Atmos. Chem. Phys.* **18**, 12491–12510 (2018).
67. Wielicki, B. A. et al. Clouds and the Earth's Radiant Energy System (CERES): Algorithm overview. *IEEE Trans. Geosci. Electron.* **36**, 1127–1141 (1998).
68. Hongyu Liu, D. J. J., Bey, I. & Yantosca, R. M. Constraints from 210Pb and 7Be on wet deposition and transport in a global three-dimensional chemical tracer model driven by assimilated meteorological fields. *J. Geophys. Res.:Atmos*. 12109–12128 (2001).
69. Wesely, M. L. Parameterization of surface resistances to gaseous dry deposition in regional-scale numerical models. *Atmos. Environ.* **23**, 1293–1304 (1989).
70. Zhang, L. M., Gong, S. L., Padro, J. & Barrie, L. A size-segregated particle dry deposition scheme for an atmospheric aerosol module. *Atmos. Environ.* **35**, 549–560 (2001).
71. McDuffie, E. E. et al. A global anthropogenic emission inventory of atmospheric pollutants from sector- and fuel-specific sources (1970-2017): an application of the Community Emissions Data System (CEDS). *Earth Syst. Sci. Data* **12**, 3413–3442 (2020).
72. Defries, R. S., Hansen, M. C. & Townshend, J. R. G. Global continuous fields of vegetation characteristics: a linear mixture model applied to multi-year 8 kmAVHRR data. *Int. J. Remote. Sens* **21**, 1389–1414 (2000).
73. Zender, C. S., Bian, H. S. & Newman, D. Mineral Dust Entrainment and Deposition (DEAD) model: Description and 1990s dust climatology. *J. Geophys. Res.:Atmos.* **108**, 4416 (2003).
74. Tian, R., Xiaoyan, M. & Zhao, J. A revised mineral dust emission scheme in GEOS-Chem: improvements in dust simulations over China. *Atmos. Chem. Phys.* **21**, 4319–4337 (2021).
75. White, B. R. soil transport by winds on Mars. *J. Geophys. Res.: Solid Earth* **84**, 4643–4651 (1979).
76. Chin, M. et al. Tropospheric aerosol optical thickness from the GOCART model and comparisons with satellite and Sun photometer measurements. *J. Atmos. Sci.* **59**, 461–483 (2002).
77. Lacis, A. A. & Oinas, V. A description of the correlated k distributed method for modeling nongray gaseous absorption, thermal emission, and multiple scattering in vertically inhomogeneous atmospheres. *J. Geophys. Res.* **96**, 9027–9063 (1991).
78. Pincus, R., Barker, H. W. & Morcrette, J. J. Afast, flexible, approximate technique for computing radiative transfer in inhomogeneous cloud fields. *J. Geophys. Res.:Atmos.* **108**, 4376 (2003).
79. Oreopoulos, L. & Mlawer, E. The continual intercomparison of radiation codes (CIRC) Assessing Anew the Quality ofGCMRadiation Algorithms. *Bull. Am. Meteorol. Soc.* **91**, 305–310 (2010).
80. Oreopoulos, L. et al. The continual intercomparison of radiation codes: results from Phase I. *J. Geophys. Res.:Atmos.* **117**, D06118 (2012).

Acknowledgements

This work is supported by the National Natural Science Foundation of China (No. 42522505, 42375092). The authors also acknowledge funding from the project supported by the Innovation Group Project of Southern Marine Science and Engineering Guangdong Laboratory (Zhuhai) (No. 311024001), the Science and Technology Planning Project of Guangdong Province (2023B1212060019, 2025B1515020034), and the Zhujiang Talent Program of the Department of Science and Technology of Guangdong Province (2017GC010619). The authors are thankful for the technical support from the National Large Scientific and Technological Infrastructure "Earth System Numerical Simulation Facility" (https://cstr.cn/31134.02.EL). F.Y. was supported by the National Environment Research Council through the National Centre for Earth Observation (#NE/R016518/1). The authors sincerely thank the three anonymous reviewers for their constructive comments and suggestions, which greatly improved the paper.

Author contributions

B.Y. and X.L. conceived the idea of this study. K.Y. designed and conducted the numerical simulations, performed the analysis, and wrote the draft paper. F.Y. provided the model framework of this study. N.L. and M.G. provided constructive suggestions on the draft paper. All authors contributed to the discussion, writing and revision of the final manuscript.

Competing interests

The authors declare no competing interests.

Additional information

Supplementary information The online version contains supplementary material available at https://doi.org/10.1038/s43247-025-03123-1.

Correspondence and requests for materials should be addressed to Xiao Lu or Bingqi Yi.

Peer review information *Communications Earth and Environment* thanks Kirsten Perry, Abdoul Aziz Saidou Chaibou and the other, anonymous, reviewer(s) for their contribution to the peer review of this work. Primary Handling Editors: Zijun Li and Nandita Basu. A peer review file is available.